



OPEN Study on the spatial mechanical behavior of the cable tower anchorage zone in long-span curved T-shaped rigid-frame extradosed bridge for high-speed railway

Mingzhi Xie^{1,2}✉, Kun Wang^{1,2}, Shijie Guo^{1,3}, Zheng Yang^{1,2}, Weiwei Bai⁴ & Xiaobin Li¹

This study investigates the spatial mechanical behavior of the cable tower anchorage zone in a long-span curved T-shaped extradosed cable-stayed bridge under operational loads, based on the case of the Changtu River Bridge on the Chongqing–Qianjiang high-speed railway. Through detailed finite element modeling, the stress distribution and load-transfer mechanism within the “raindrop-shaped” strand-guiding saddle anchorage are analyzed. Key findings reveal a parabolic distribution of vertical stress in both the high-strength grout and the concrete below the saddle, with significant load concentration in the curved arc segment. Vertical tensile stresses generated above the saddle may adversely affect the bonding interface. Transverse splitting stresses exhibit distinct “M-shaped” and “W-shaped” patterns at depths of 0.8–1.2 m and 0–0.8 m, respectively. Parametric analysis indicates that the principal tensile stress in the grout decreases with larger saddle arc radius r but increases linearly with the cable force increment ratio λ . Conversely, the vertical compressive stress in the concrete beneath the saddle is inversely related to r and directly proportional to λ . An optimal saddle arc radius between 5 and 5.5 m is proposed to mitigate stress concentrations and improve mechanical performance. These results provide valuable insights for the design and construction of anchorage systems in extradosed cable-stayed bridges subjected to complex spatial load conditions.

Keywords High-speed railway, Extradosed cable-stayed bridge, Cable tower anchorage zone, Stress characteristic, Force transmission characteristics, Parametric analysis

An extradosed cable-stayed bridge is a hybrid system that lies between beam bridges and traditional cable-stayed bridges, offering advantages such as cost-effectiveness, high structural stiffness, and favorable aesthetics. In recent years, its application in high-speed railway bridges has become increasingly widespread^{1–4}. The anchorage zone of the tower is a critical node where the interaction between the cable and tower occurs, and it experiences complex forces. Additionally, under the action of cable forces, the concrete in the anchorage zone is subjected to significant compressive and lateral splitting stresses, making it prone to cracking^{5–8}. Moreover, the structural form of the strand-pipe and saddle significantly influences the stress distribution in the anchorage zone of extradosed cable-stayed bridges⁹. The development of the through-type strand-pipe saddle for extradosed cable-stayed bridges has evolved through several stages, including “circular,” “raindrop,” and “diamond” shapes^{10,11}. Among these, the “raindrop-shaped” strand-pipe is particularly effective in distributing stresses in the anchorage zone and offers improved anti-sliding performance, making it more suitable for long-span bridges. However, the application of the “raindrop-shaped” strand-pipe saddle in long-span extradosed cable-stayed bridges is still in its early stages, and further clarification of its mechanical behavior is needed. Therefore, an in-depth

¹School of Civil Engineering, Southwest Jiaotong University, Chengdu 610031, Sichuan, China. ²State Key Laboratory of Bridge Intelligent and Green Construction, Southwest Jiaotong University, Chengdu 610031, Sichuan, China. ³Shudao Investment Group Co., Ltd., Chengdu 610041, Sichuan, China. ⁴The Third Engineering Co., Ltd of China Railway Seventh Group, Zhengzhou 450016, Henan, China. ✉email: xiemingzhi@126.com

investigation into the structural parameters, spatial stress distribution, and force transfer characteristics of this type of saddle is of both theoretical and practical significance.

Scholars both domestically and internationally have conducted various studies on the mechanical behavior of the cable tower anchorage zone through theoretical derivations, numerical analyses, and model experiments. In terms of the force characteristics of the anchorage zone, Li et al.¹² focused on the high-density polyethylene (HDPE) multitube saddle structure and cement slurry filling, the mechanical properties of the saddle are analyzed and verified in detail by a full-scale model test. It is shown that the saddle structure design is safe and that the saddle structure meets the design requirements. Based on the main bridge of the Paira Bridge in Bangladesh, Wang et al.¹³ studied the behavior of a multi-span extradosed bridge under variations in cable-free segment length. The results showed that changes in cable-free segment length had a significant impact on the horizontal displacement of the pylon top and the vertical displacement at the midspan of each span. To gain a deeper understanding of the fatigue behavior of these anchorage systems, Chehrazi et al.¹⁴ conducted a research project in which fatigue tests were performed on saddle test specimens. Additionally, analytical models were developed to calculate displacements and contact forces, and a multiaxial stress-based fretting fatigue model was proposed to estimate fatigue life. Tang et al.¹⁵ conducted comparative calculations on the strand-pipe anchorage zone using the finite difference method (FDM) and finite element method (FEM). The results indicated that, except for the loading area, the FDM's approximate solutions could enhance computational efficiency when compared to FEM solutions. Niu et al.¹⁶ simulated the temperature distribution in both the transverse and longitudinal directions of the bridge when the maximum negative temperature difference occurred in solid concrete bridge towers and derived the corresponding curve equation. Lou et al.¹⁷, based on theoretical analysis, proposed a Ritz method for studying the mechanical behavior of asymmetric extradosed cable-stayed bridges. Compared with traditional force methods, displacement methods, or FEM, the Ritz method is simpler and more efficient when solving equations. Liu et al.¹⁸, using the main bridge of the Jinghu high-speed railway Tianjin-Hu Railway Link as a case study, conducted model experiments and finite element theoretical analysis to study the stress distribution and crack-prone areas of the concrete in the cable tower anchorage zone. They found that the longitudinal and transverse stresses in the concrete beneath the saddle exhibited a parabolic distribution, with transverse tensile cracking being more likely. The authors suggested increasing the reinforcement density in this area during design. Tang et al.¹⁹ investigated the force mechanism of the cable tower anchorage zone in extradosed cable-stayed bridges through formula derivation, finite element simulation analysis, and segmental model experiments, revealing the stress state and distribution patterns of the concrete beneath the strand-pipe saddle. Current studies primarily focus on highway bridges, often analyzing the concrete stress distribution around the saddle in segmental models, with the "circular" strand-pipe structure commonly used for cable saddles. Research on the "raindrop-shaped" strand-pipe saddle remains limited, and its force state, structural parameters, and force transfer characteristics in the anchorage zone under the combined effects of tower and cable loads need to be clarified. Additionally, unlike highway extradosed cable-stayed bridges, railway bridges must bear greater loads, and the overall force conditions become more complex due to the influence of track curvature. This imposes higher demands on the saddle structure and performance. The "raindrop-shaped" saddle demonstrates excellent anti-sliding and cable force distribution capabilities, but because it directly bears the cable forces, it is necessary to further investigate its performance and structural parameters' effects on the overall bridge structure. Therefore, studying the spatial stress distribution in the anchorage zone, the structural parameters of the strand-pipe saddle, and the force transfer characteristics in the anchorage zone for this type of extradosed cable-stayed bridge has both theoretical and practical significance.

This study investigates the spatial mechanical behavior of the anchorage zone in a long-span curved T-shaped rigid-frame extradosed cable-stayed bridge, with a (132 + 132) m span, located on the Chongqing to Qianjiang section of the Yuxiang high-speed railway. Using finite element numerical simulations, the stress distribution patterns in the concrete beneath the "raindrop-shaped" high-strength grouted strand-pipe saddle and the saddle itself are analyzed. The load transfer paths and distribution ratios are identified, and the impact of variations in the saddle's arc radius and cable force on the anchorage zone's stress distribution is clarified through parameter analysis. These findings offer critical insights for the design of similar strand-pipe saddles and for the construction control of extradosed cable-stayed bridges. The three-dimensional model of the bridge is illustrated in Fig. 1.

The establishment of a spatial finite element model

Project overview

The newly constructed Changtu River Bridge on the Chongqing to Qianjiang high-speed railway features a single-tower, double-cable-plane T-shaped curve extradosed cable-stayed bridge with spans of (132 + 132) meters. The bridge is located on a curve with a radius of $R = 8000$ m, along a transition curve, and is designed for a speed of 350 km/h, with a design load of double-line ZK live load. The bridge adopts an inverted "Y"-shaped tower, with a tower height of 38 m. A total of 9 pairs of stay cables (18 groups) are arranged, and the stay cables are made of 1860 MPa galvanized steel strands. The main bridge has a total length of 265.7 m, and the main girder uses a single-box, double-chamber variable-height straight web plate cross-section. The top width of the box girder is 14.3 m, the bottom width is 11.3 m, and the height at the mid-span is 13.0 m, with the height at the edge spans being 7.0 m. The cross-section height varies according to the circular curve radius $R = 887.08$ m, with the top slab thickness being 45 cm and the bottom slab thickness ranging from 50 to 100 cm, with the thickness varying along the curve. The bottom slab has a top curve radius of $R = 967.21$ m, and the web thickness varies from 50 to 75 to 90 cm, following a linear change across three segments. The elevation layout of the main bridge is shown in Fig. 2a. The anchorage zone of the stay tower uses a "raindrop" shaped strand-pipe saddle, with the external layer of the saddle made of a steel shell structure that wraps around the strand pipes with high-strength grout. The steel shell of the saddle is box-shaped, constructed from Q355B steel, and features a design that includes a linear segment + arc segment + linear segment. The saddle is filled with high-strength grout, with a

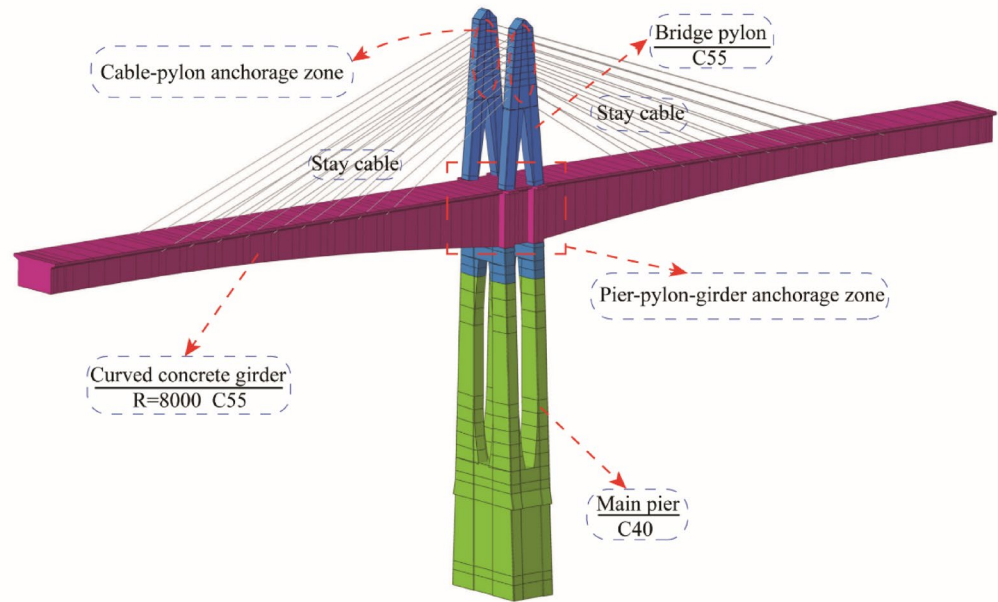


Fig. 1. 3D schematic diagram of an extradosed cable-stayed bridge.

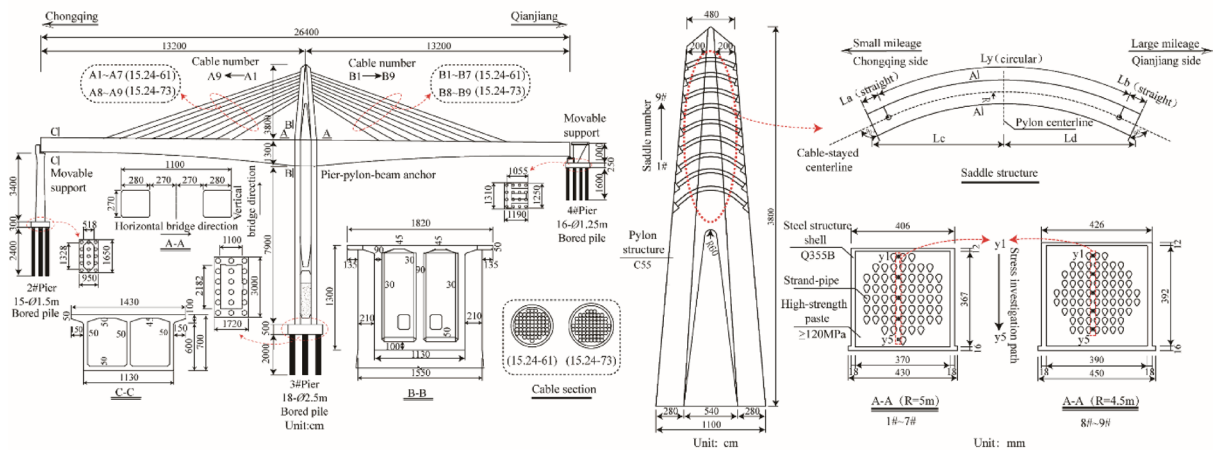


Fig. 2. Engineering profile drawing.

cubic compressive strength of no less than 120 MPa. The strand-pipe saddle consists of two types of holes: 61 holes and 73 holes, with the arc radii being 500 cm and 450 cm, respectively. The cross-sections of the bridge tower, saddle, and strand pipes are shown in Fig. 2b.

Principle of equivalent load calculation

Accurate determination of cable force application methods, load quantification, and equivalent loading constitutes the essential foundation for anchorage zone analysis in cable-stayed tower structures. In this study, cable forces are transferred to strand-pipe contact surfaces through steel strand holes using an equivalent load distribution approach. The global bar-system bridge model analysis reveals uniform cable force distribution across saddle regions under service conditions, with negligible effects from force imbalance (unconsidered in this investigation). Following established methodologies¹⁹, the normal force acting on strand-pipes originates from tangential forces generated by steel strands traversing the saddle arc. Key analytical assumptions include: Uniform longitudinal normal stress distribution along the saddle arc section; Equal force allocation to each strand-pipe hole proportional to hole quantity; Identical load magnitude/direction for all holes within individual saddle units. For a system containing n strand-pipe holes, mechanical analysis is conducted on a representative micro-segment of the strand-pipe assembly (see Fig. 3), enabling systematic evaluation of force transmission characteristics.

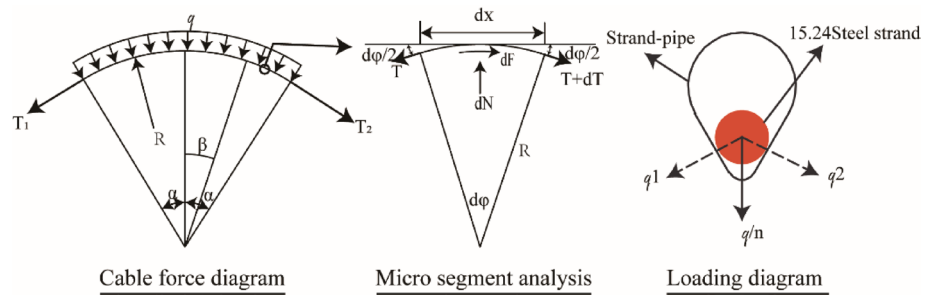


Fig. 3. Saddle loading analysis.

$$dN = qdx = T \sin \frac{d\varphi}{2} + (T + dT) \sin \frac{d\varphi}{2} \approx Nd\varphi \tag{1}$$

where q represents the linear load intensity applied by the stay cable on the strand-pipe stay saddle. x represents the length of the arc micro-segment of the strand-pipe. $d\varphi$ represents the angle subtended by the arc micro-segment of the strand-pipe. T represents the tensile force in the stay cable.

Let μ represent the friction coefficient between the stay cable and the stay saddle. Then, the tangential friction force dF between the micro-segment of the steel strand dx and the duct can be obtained by using Eq. (2)

$$dF = f dx = q\mu dx = \mu N d\varphi \tag{2}$$

In the equation, f represents the total frictional force per unit length exerted by the stay cable on the inner wall of the strand pipe. The axial force equilibrium of the micro-segment of the stay cable leads to the following Eq. (3).

$$T + dT + dF = T \tag{3}$$

$$dF = -dT = \mu T d\varphi \tag{4}$$

$$\frac{dT}{T} = -\mu d\varphi \tag{5}$$

Integrating both sides of Eq. (5) gives (6).

$$T = -\mu d\varphi + c \tag{6}$$

where c represents the constant of integration. By applying the boundary conditions, when the calculation section coincides with the tension side, φ takes the value φ_0 and the tensile control force of the stay cable is T_{con} . Thus, $\varphi = \varphi_0 = 0$ and $T = T_{con}$. Substituting these conditions into Eq. (6) yields the integration constant $c = \ln T_{con}$.

$$\ln T = -\mu d\varphi + \ln T_{con} \tag{7}$$

Integrating both sides of Eqs. (7) gives (8).

$$T = T_{con} e^{-\mu\varphi} \tag{8}$$

Substituting the result of Eq. (8) into Eq. (1), the axial pressure dN can be derived using Eq. (9).

$$dN = T_{con} e^{-\mu\varphi} d\varphi \tag{9}$$

By introducing the relationship for a small angle, $d\varphi = \frac{1}{R} dx$, where R represents the radius of the saddle arc segment, Eq. (1) can be expressed as $q = dN/dx$. Substituting Eq. (9) yields the distributed load per unit length, q .

$$q = \frac{T_{con} e^{-\mu\varphi}}{R} \tag{10}$$

In Eq. (10), neglecting the effect of the friction coefficient ($\mu = 0$), the distributed load per unit length simplifies to $q = \frac{T_{con}}{R}$. The vertical component of the distributed load is applied to the sidewalls of the strand-pipe holes, while the transverse component is determined using the resultant force theorem, leading to Eq. (11).

$$q_1 = q_2 = \frac{q}{ns} = \frac{T_{con}}{Rns} \tag{11}$$

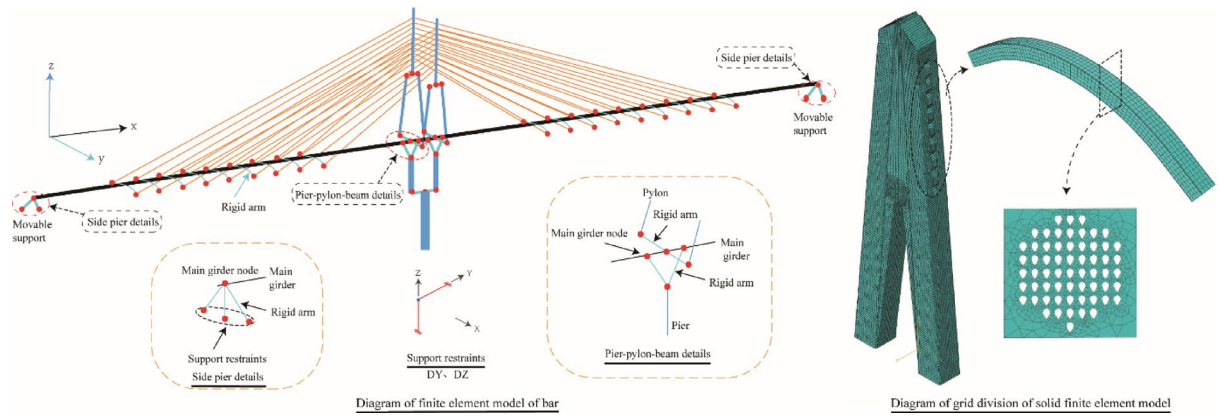


Fig. 4. Finite element modeling.

Model type	Support reaction (kN)	Axial stress in bridge tower (MPa)
Solid finite element model of the bridge tower	3.19E+05	-4.12
Full-bridge beam-element model	3.15E+05	-4.1
Modeling error	1.27%	0.49%

Table 1. Deviation in Calculation Results between the Bridge Tower Solid Model and the Full-Bridge Beam-Element Model.

where q_1 and q_2 represent the equivalent surface loads applied to the loading faces of the strand-pipe holes; s represents the width of the loaded surface of the strand-pipe holes, taken as 14 mm; and n represents the number of holes, which includes 61 and 73 holes.

Finite element modeling

To systematically investigate the spatial mechanical behavior of the cable tower anchorage zone in a long-span curved extradosed cable-stayed bridge with T-shaped rigid frame for high-speed railways, this study employed a multi-scale numerical approach. A global beam-element model was first established in Midas/Civil, simulating main girders and pylons with beam elements while representing stay cables as tension-only truss elements with initial prestress forces. Operational stage cable forces derived from this model were subsequently applied as boundary conditions for a localized refined analysis. Focusing on the exterior-curvature side (subjected to higher cable forces), a 38 m-high solid-element pylon model above the deck was developed in ABAQUS, incorporating three key components: pylon concrete (meshed at 200 mm), steel saddle structures (100 mm), and high-strength grout in tendon ducts (50 mm). The model comprised 1,781,412 elements (C3D8R/C3D6) with 1,261,223 nodes, utilizing Tie constraints at steel-concrete interfaces while neglecting minor simulation-actual condition discrepancies. The full-bridge bar system model and the local entity model of the cable tower are shown in Fig. 4.

Validation procedures ensured model reliability through systematic comparisons with global analysis results. Boundary conditions and loading protocols were rigorously derived from the beam-model outputs, with verification metrics including stress distributions at critical pylon sections and axial forces at the tower base (corresponding to solid-model support reactions). As shown in Table 1, the solid model demonstrated excellent agreement (<2% discrepancy) with beam-model predictions, confirming its fidelity for subsequent mechanical investigations.

Analysis of spatial mechanical characteristics in the cable tower anchorage zone

Spatial stress characteristics of the anchorage zone

To address the complex spatial stress state in the pylon anchorage zone of the extradosed cable-stayed bridge, a systematic stress analysis was conducted on three critical components: high-strength grout in tendon ducts, steel saddle structures, and pylon concrete. Given the repetitive configuration of saddle assemblies (Saddles #1–#7 sharing identical specifications, while #8–#9 featuring increased cable strands), five representative saddle pairs (#1, #4, #7, #8, and #9) were selected for detailed evaluation. Their principal stress states (σ_1 and σ_3), vertical normal stresses, and critical stress zones are summarized in Table 2, with corresponding stress contours illustrated in Figs. 5 and 6.

Numerical simulations revealed that the grouted tendon ducts exhibited maximum principal tensile and compressive stresses of 5.04 MPa (Saddle #9) and -7.91 MPa (Saddle #2), respectively, both below the material strength design thresholds (120 MPa). Vertical stress analysis identified peak compressive stress (-8.43 MPa) at the inter-duct wall of Layer 8 in Saddle #1, while maximum tensile stress (4.94 MPa) occurred at the duct wall of Layer 1 in Saddle #9.

Component	Stress results				Most unfavorable loading position	
	Max principal	Min principal	Vertical normal stress	Von mises		
1#	Steel shell structure	1.66 ~ 3.60	- 15.79 ~ 0.76	- 16.47 ~ - 0.34	16.27	Straight segment web
	High-strength grout	- 1.01 ~ 2.64	- 7.76 ~ 0.13	- 8.43 ~ - 0.02	6.75	Lower edge of the topmost strand-pipe hole row
4#	Steel shell structure	- 0.40 ~ 4.86	- 10.72 ~ 0.22	- 10.34 ~ 0.12	10.45	Straight segment web
	High-strength grout	- 0.89 ~ 2.56	- 6.23 ~ 0.24	- 6.13 ~ 0.64	5.32	Junction between the straight segment and the curved segment
7#	Steel shell structure	- 0.22 ~ 3.98	- 6.53 ~ 0.30	- 6.01 ~ - 0.52	6.36	Straight segment web
	High-strength grout	- 0.90 ~ 4.09	- 4.97 ~ 0.36	- 4.88 ~ - 2.28	5.26	Between the topmost strand-pipes in the curved segment
8#	Steel shell structure	- 1.29 ~ 2.88	- 5.81 ~ 0.26	- 4.86 ~ 1.09	6.36	Web at the junction of the straight and curved segments
	High-strength grout	- 1.04 ~ 3.84	- 4.97 ~ 0.44	- 4.92 ~ 3.26	5.45	wall of the second row of strand-pipe holes at the junction of the straight and curved segments
9#	Steel shell structure	- 0.52 ~ 4.63	- 3.82 ~ 0.05	- 2.76 ~ 2.09	5.79	Middle of the top slab in the curved segment
	High-strength grout	- 1.20 ~ 5.04	- 4.94 ~ 0.63	- 4.83 ~ 4.94	5.00	Between the second row of strand holes at the middle of the arc segment
Anchorage zone concrete	- 3.72 ~ 1.76	- 5.089 ~ - 0.01	- 4.91 ~ 1.03	4.56	Fork of the bridge tower	

Table 2. Stress distribution in anchoring area (MPa).

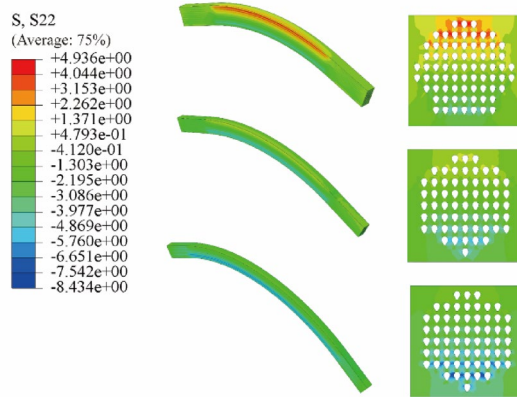


Fig. 5. Vertical stress nephogram of high strength slurry of pipe (MPa).

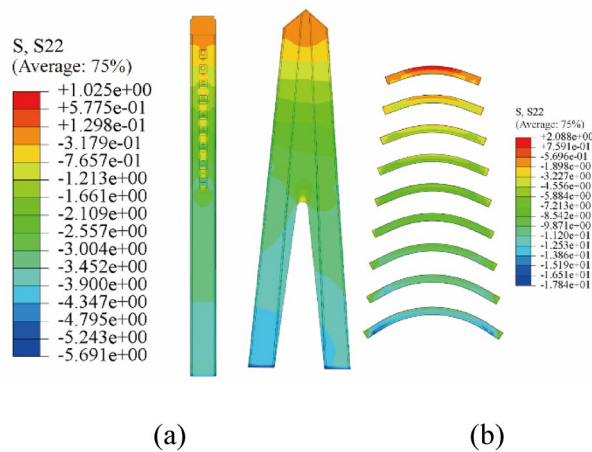


Fig. 6. Vertical stress nephogram of bridge tower and cable saddle steel shell (MPa). (a) The bridge tower, (b) Saddle steel shell.

The stress distribution characteristics demonstrated significant inhomogeneity due to the perforated cross-sections of grouted ducts. Vertical stress gradients exhibited progressive amplification toward the pylon apex, with compressive stresses accumulating downward along the saddle height due to load superposition effects. Notably, duct walls – identified as structural weak points – displayed pronounced stress concentrations. To elucidate vertical stress propagation patterns along both longitudinal (pylon axis, $x=0$) and vertical directions, five critical paths ($y_1 \sim y_5$, see Fig. 2) across duct walls were analyzed for Saddles #1, #4, and #7, as depicted in Fig. 7.

Figure 7 reveals stratified vertical stress distributions along predefined paths within the grouted ducts, demonstrating position-dependent uniformity across curved segments. Adjacent paths (1–4) exhibited comparable vertical stress differentials with progressive escalation (e.g., stress increments of 1.32 MPa, 1.61 MPa, and 1.64 MPa between consecutive paths at Saddle #1). A notable stress mitigation occurred between Paths 4–5, attributed to reduced perforation density (-0.41 MPa increment at Saddle #1 vs. 0.7 MPa at Saddle #7). These findings quantitatively confirm the critical influence of tendon duct configuration on stress evolution, suggesting optimized perforation design as an effective strategy for stress homogenization. Transitional stress discontinuities emerged at curve-to-linear segment interfaces, with path stresses converging to uniform values in linear regions before decaying linearly toward null states with increasing $|x|$. Linear segment stresses primarily originated from gravitational effects and layered cable force diffusion, maintaining minimal height-direction variation and enhanced uniformity within saddle zones.

Under operational loading, Saddle #7 exhibited tensile stresses ranging $1.7\text{--}0.2$ MPa along Paths 1–2, induced by steel-grout interfacial bonding. Analytical results indicate that 74.3% of upper cable forces (Rows 1–3) were equilibrated through top-edge bonding constraints, while compressive dominance in Paths 3–5 confirmed force transfer to saddle sidewalls and basal concrete. The vertical stress distribution across multiple saddles further revealed a cumulative effect of cable forces from top to bottom: saddle #7 at the top exhibited tensile stress along path Y1 due to deformation compatibility under lower compressive confinement, whereas saddles at lower levels (e.g., #4 and #1) experienced a transition from tensile to compressive stresses, with near-zero stress occurring around saddle #4. This linear stress distribution explains the higher absolute stress value in saddle #7 compared to #4 and #1, as observed in Fig. 7c versus Fig. 7a and Fig. 7b. Comparative analysis also highlighted stress redistribution mechanisms: superposition of vertical cable components promoted steel–concrete deformation compatibility, with concrete-derived compressive forces neutralizing bond-induced tensile stresses. This explains the reduced tensile stress at Saddle #4 (0.35 MPa at Y1) versus Saddle #7 (1.8 MPa). As Table 2 indicates, persistent principal tensile stresses (up to 5.04 MPa) necessitate anti-cracking measures in grout design, particularly given their proximity to material strength thresholds.

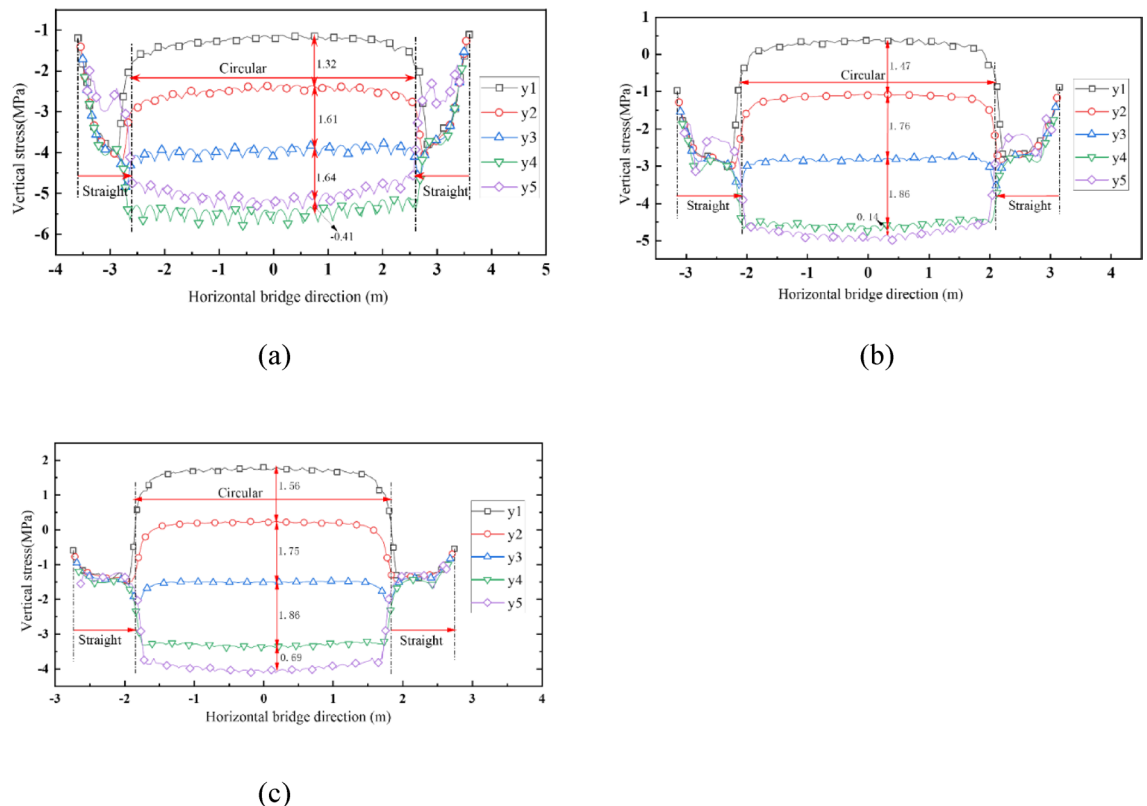


Fig. 7. Vertical stress distribution in high-strength grout. (a) 1# Strand-pipe of saddle, (b) 4# Strand-pipe of saddle, (c) 7# Strand-pipe of saddle.

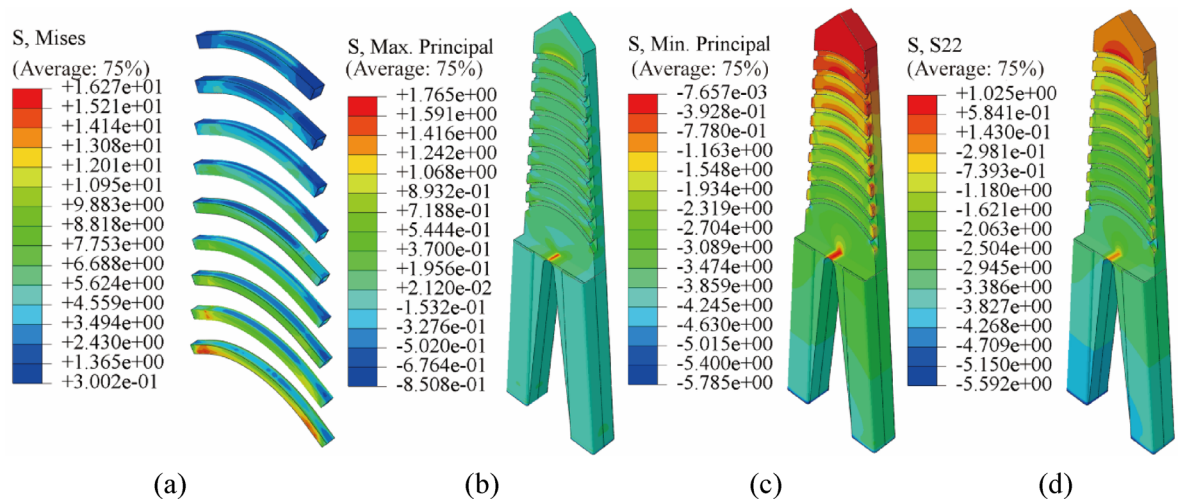


Fig. 8. Stress distribution cloud diagram of concrete of rigid shell and bridge tower. (a) Von mises of steel shell structure, (b) Max principal of tower, (c) Min principal of tower, (d) Vertical normal stress of tower.

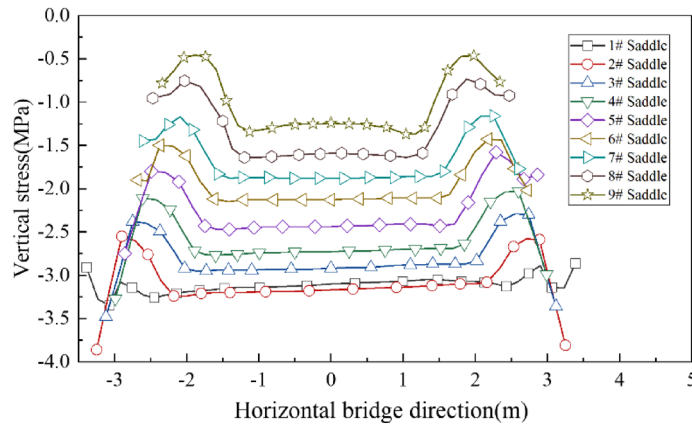


Fig. 9. Stress distribution of concrete under saddle (MPa).

Steel saddle analysis (Fig. 8a) identified peak von Mises stress (16.27 MPa) at Saddle #1's web linear segment, well below the design strength (325 MPa) of Q355b steel, suggesting material optimization potential. Concrete evaluation (Fig. 8b and c) within the upper pylon (20.32 m below apex) showed principal tensile and compressive stresses of 1.77 MPa and -5.09 MPa, respectively, both within C55 concrete elastic limits. Simultaneously, Fig. 8d demonstrates that the pylon is predominantly subjected to vertical compressive stresses, with maximum tensile and compressive stress components of 1.03 MPa and 5.59 MPa, respectively, along the vertical direction. Critical stress concentrations were observed at: Anchorage notches (compressive); Y-shaped bifurcations (tensile, 1.77 MPa vs. design strength 1.96 MPa). Notably, the 9.7% safety margin at bifurcations warrants reinforced detailing to mitigate cracking risks.

Figure 9 illustrates the longitudinal distribution of vertical compressive stress at the concrete-saddle interface, with saddle numbering consistent with Fig. 2. The vertical stress exhibits a characteristic "U"-shaped symmetric profile along the radial direction within the curved segments, accompanied by a uniform compressive stress distribution inside the arc zones. A noticeable reduction in compressive stress occurs at the transition between curved and straight segments, resulting in relatively lower stress levels within the straight portions. Further outward, localized stress intensification is observed due to the "L"-shaped obtuse-angle openings at the anchor notch, indicating mild stress concentration.

Under the action of cable forces decreasing progressively from saddle #9 (8950 kN) to #1 (6699 kN), the vertical compressive stress beneath the saddles accumulates gradually. Notably, the difference in vertical stress between adjacent saddles diminishes toward the lower region of the anchorage zone. This convergence behavior—particularly the nearly identical stresses under saddles 1 and 2—is attributed to the combined effect of reducing cable forces and increasing cross-sectional area of the pylon. When the decrease in cable force is insufficient to counteract the enhanced sectional stiffness, the stress distribution becomes uniform near the base. The stratified and parallel stress contours suggest significant superposition effects and confirm that the pylon remains within the elastic range under the applied loads.

Transverse distribution pattern of concrete stress beneath the saddle

The preceding analysis reveals that the concrete beneath cable saddles experiences a complex three-dimensional stress state with relatively high stress magnitudes, necessitating comprehensive investigation into its structural mechanical behavior. Previous studies²⁰ have demonstrated that extradosed cable-stayed bridge saddles may develop splitting cracks propagating along tendon ducts under cable force actions. To systematically evaluate the transverse stress distribution patterns in saddle-underlying concrete and quantify potential splitting effects on pylon concrete, three representative saddles (#1, #5, and #9) were selected for targeted analysis. Figure 10 illustrates the transverse distribution of vertical stresses within a 1.2 m vertical range below these saddles, where $x=0$ corresponds to the pylon's longitudinal axis and y denotes the lateral distance from measurement points to the saddle base.

Figure 10a–c reveal parabolic symmetrical stress distributions beneath the saddles, with intersecting stress contours at $x = \pm 400$ mm for Saddles #5 and #9. Beyond $x = \pm 400$ mm, these contours transition to stratified parallel patterns extending to ± 1150 mm. At Saddle #1 near the pylon's Y-shaped bifurcation, maximum vertical compressive stress (-3.2 MPa) occurs at the saddle-concrete interface ($y=0.0$ m). The 1.2 m analysis zone beneath Saddle #1 exhibits pronounced stress gradients ($\Delta \sigma(\max) = 2.8$ MPa) between $x = -400$ mm and 400 mm, contrasting with the relatively uniform distributions observed at Saddles #5 and #9. As shown in Fig. 10d, stress redistribution toward the bifurcated limbs induces height-direction homogenization (variation coefficient $< 8\%$) beneath Saddle #1, with subsequent stress increments primarily governed by self-weight superposition.

Due to the direct action of cable forces, the local compressive deformation of the saddle is greater than that of the surrounding tower concrete. Owing to the deformation compatibility of the concrete within the local region of the saddle, the compressive strain in the concrete around Saddle #1 to #8 is smaller than that on both sides. As a result, for Saddle #5 and #9, when y is approximately 1.2 m, the compressive stress within the range of $x = -400$ to 400 mm is lower than that at the edges, as shown in Fig. 9e and f.

Meanwhile, when the compressive deformation of the concrete above the saddle is less than the local deformation of the saddle itself, tensile stress develops vertically in the upper part of the saddle. For instance, in Fig. 9c, a tensile stress of 0.43 MPa is observed above Saddle #9 at $y=1.0$ – 1.2 m. Excessive deformation differences may cause the vertical tensile stress to exceed the bond stress between the saddle and the tower concrete, leading to potential debonding at the top plate of the steel shell box of the saddle and cracking of the concrete. The maximum vertical tensile stress, reaching 1.03 MPa, is located in the concrete above Saddle #9, as illustrated in Fig. 9f. Special attention should be paid to the stress state in this region during design and construction, and appropriate reinforcement measures should be considered.

Through understanding the lateral distribution pattern of the vertical compressive stress in the concrete beneath the saddle, in order to further explore the mechanical characteristics of the anchorage zone and reveal the impact of transverse splitting stress induced by vertical compressive stress on the concrete beneath the saddle, this paper will further analyze the distribution and effect of transverse splitting stress. In-depth analysis

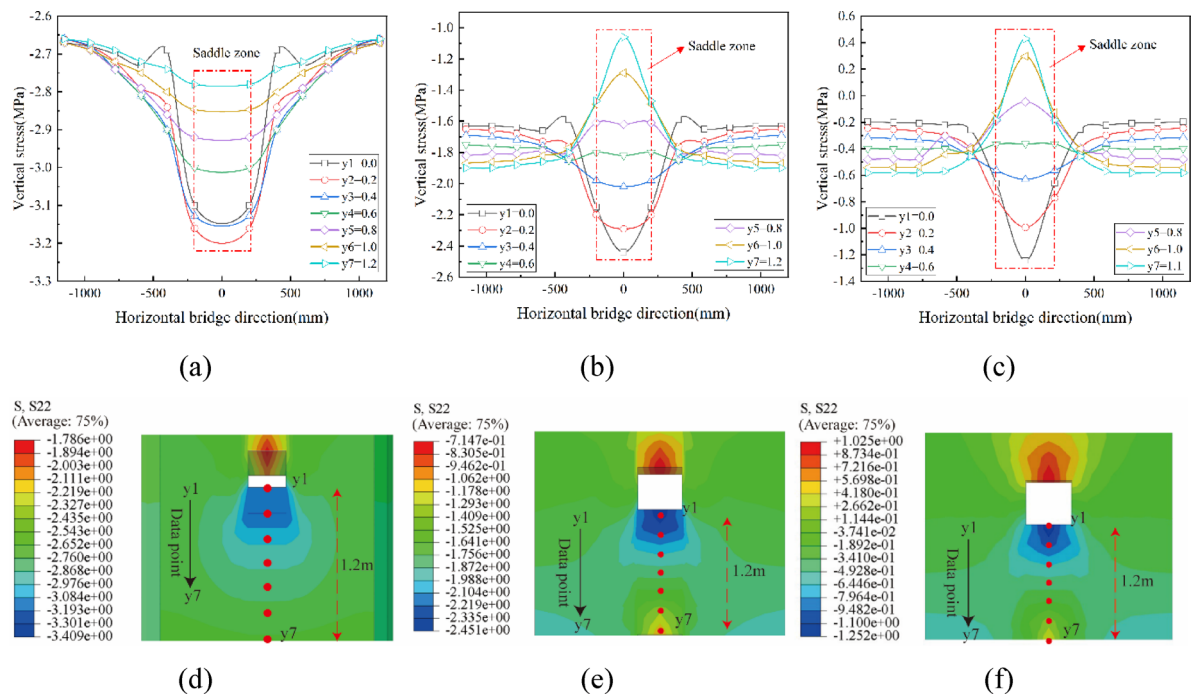


Fig. 10. Transverse distribution of vertical stress in concrete under saddle. (a) 1# Strand-pipe of saddle, (b) 5# Strand-pipe of saddle, (c) 9# Strand-pipe of saddle, (d) Cloud diagram of 1# saddle, (e) Cloud diagram of 5# saddle, (f) Cloud diagram of 9# saddle.

of the splitting stress distribution can provide theoretical support for structural design optimization, ensuring the safety and reliability of the structure under load.

Figure 11 shows the lateral distribution of splitting stress in the concrete beneath the saddle. From the stress cloud diagrams in Fig. 11d and e, it can be seen that the concrete mainly experiences tensile stress, which diffuses radially from the center towards both sides in a ring-like pattern, with an expansion angle of approximately 45°. The concrete splitting stress (lateral tensile stress) gradually increases within the range of 0–0.4 m from the bottom edge of the saddle and reaches its peak. The affected area is approximately a curved square shape, and after transmitting downward, it decreases gradually. The stress distribution shows a distinct layering effect, as shown in Fig. 11b and c. The maximum tensile stress occurs in the range of 0.2–0.6 m beneath the 1# saddle of the strand tube, approximately 0.11 MPa, which is far below the allowable tensile stress of the concrete. The affected area is relatively small, and the concrete's crack resistance in the anchorage zone meets the requirements.

Due to the vertical spacing of the saddles being 1.2 m, the stresses in the strand tubes corresponding to $h=1.2$ m in Saddles 5# and 9# are exactly the same as the lateral stresses at the contact interface between the top plate of the steel shell of Saddles 4# and 8# and the concrete of the tower, as shown in Fig. 11b and e. Affected by the load from the lower strands, the concrete stress curves in Saddle 5# from $h=0.8$ m to 1.2 m show an "M"-shaped distribution, while the upper part of Saddle 4# in the range of $h=0.4$ m displays lateral compression, and after extending to both sides, it transforms into a tensile state. The stress curve at $h=0$ m is exactly the opposite, exhibiting a "W"-shaped distribution. It is important to note that while these specific stress distributions are complex, the mechanical resistance of the anchorage zone is primarily governed by inherent structural properties, such as the concrete grade and reinforcement ratio. As indicated by the numerical results, the maximum lateral tensile stress induced by these patterns is 0.13 MPa (Fig. 11), which is significantly lower than the design tensile strength of the C55 concrete (1.96 MPa). Therefore, the structural capacity of the anchorage zone is more than adequate. Due to the combined lateral and vertical forces acting on the sidewall concrete from the saddle, a lateral compressive stress region is formed at a 45° downward angle on the sidewall. From $h=0-0.4$ m, and in the symmetric region $x=400-1150$ mm, the concrete experiences compressive stress while also inducing lateral tensile stress at the top of the saddle. Therefore, during design, it is advisable to consider increasing reinforcement in the tensile region to prevent concrete cracking.

Spatial force transfer mechanism in the anchorage zone

Unlike traditional parallel-guided strand tube saddles, the anchorage zone of this bridge tower primarily consists of the high-strength grout, the steel shell structure, and the surrounding concrete on the saddle. The cable force directly acts on the side of the strand tubes, diffusing the load through the high-strength grout in the saddles, and then transferring it to the four contact surfaces of the saddle through the box-shaped steel shell structure. Due to the superimposed effects of the load, the load transfer ratio for each strand tube saddle differs, and the equivalent load of the cable force is directed toward the center of the arc segment of the saddle. The load

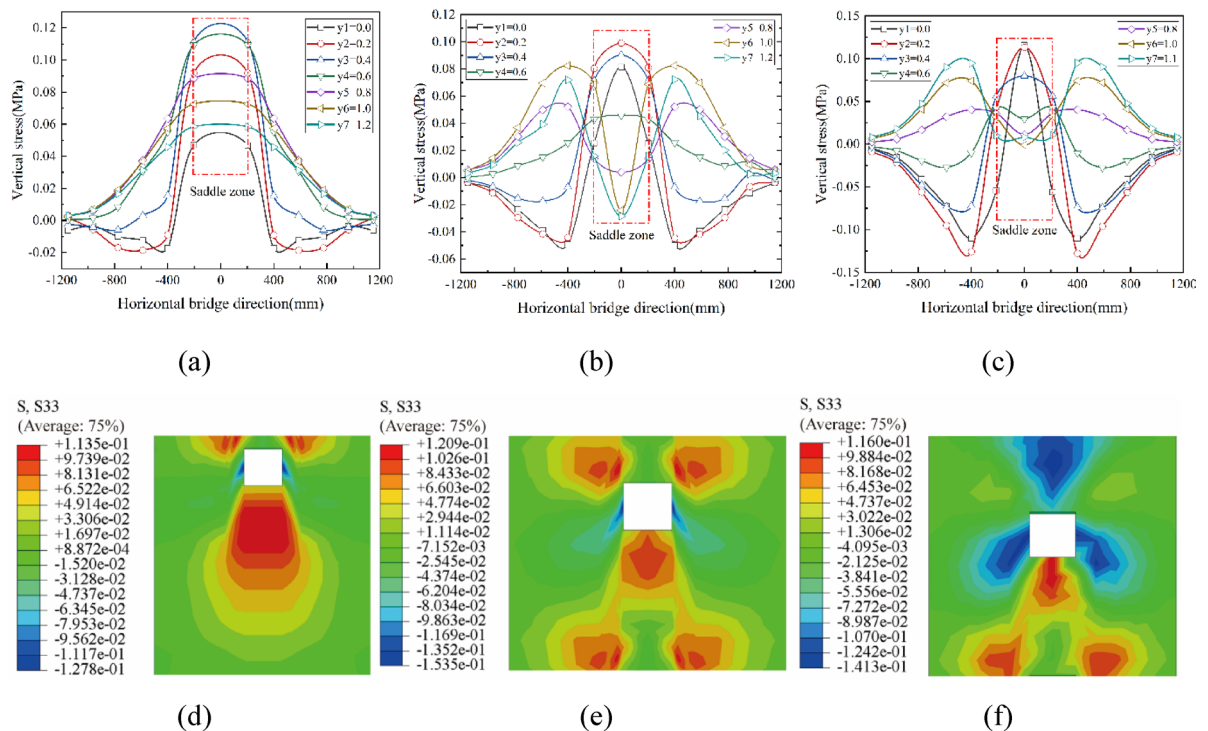


Fig. 11. Transverse distribution of concrete splitting stress beneath the saddle. (a) 1# Strand-pipe of saddle, (b) 5# Strand-pipe of saddle, (c) 9# Strand-pipe of saddle, (d) Cloud diagram of 1# saddle, (e) Cloud diagram of 5# saddle, (f) Cloud diagram of 9# saddle.

Cable saddle number	Box-type steel shell			
	Top slab (%)	Bottom slab (%)	Web 1 (%)	Web 2 (%)
1#	0	16	42	42
2#	0	16	42	42
3#	0	17	43	39
4#	0	18	41	41
5#	0	20	40	40
6#	0	20	40	40
7#	0	21	39	39
8#	7	28	32	33
9#	34	53	6	6

Table 3. Load distribution ratio on the cable saddle bearing surface.



Fig. 12. Saddle installation.

transfer paths on different segments of the same saddle and the load distribution on its four surfaces will exhibit significant differences.

The structure of the anchorage zone mainly bears vertical compressive stress under the action of the cable force. The previous analysis shows that the vertical stress distribution in the saddle's arc segment is uniform, so the primary analysis focuses on the vertical load distribution on the four plates of the box-shaped steel shell along the centerline of the bridge tower, as shown in Fig. 2. Based on the finite element calculation results, the stress along the vertical direction of the selected cross-sections of each plate is integrated, and the internal force ratio of each plate is calculated. This allows for a quantitative analysis of the load transfer mechanism between the components of the saddle in the anchorage zone. The load-bearing ratio coefficient is calculated using Eq. (12).

$$\alpha = \frac{t \int_0^l s(l) dl}{\sum t \int_0^l s(l) dl} \times 100 (\%) \quad (12)$$

where t represents the thickness of each plate, l represents the length of the end section of each plate, s represents the stress along the vertical direction at the nodes of the end section of each plate.

For the vertical force, it manifests as shear stress on the two web plates, while it acts as surface pressure on the top and bottom plates. The load distribution ratios for 1# to 9# saddle seats are shown in Table 3, with the finite element calculation diagrams and the sectional area percentage curves illustrated in Fig. 13. During the bridge erection process, the saddle is positioned and installed using a rigid framework, as shown in Fig. 12.

For the local structure of the anchor zone of the cable-stayed tower, the load transfer path is as follows: stay cable to high-strength grout in the strand tube to steel shell to bridge tower concrete. As shown in Table 3 and Fig. 13, the load from the stay cables at 1# to 7# saddle seats is primarily transmitted through the web plates of the box-type steel shell to the concrete of the bridge tower after passing through the high-strength grout. The load transfer between the two web plates is almost identical, with each web plate carrying approximately 40% of the load. The load distribution on the bottom plate increases slightly, reaching about 20%, for the 1# to 7# saddle seats, due to the cumulative load effect. The top plate mainly bears the compressive stress transferred by the upper concrete, so the load transfer from the grout to the top plate is negligible, at 0%, for the 1# to 7# strand tube saddles.

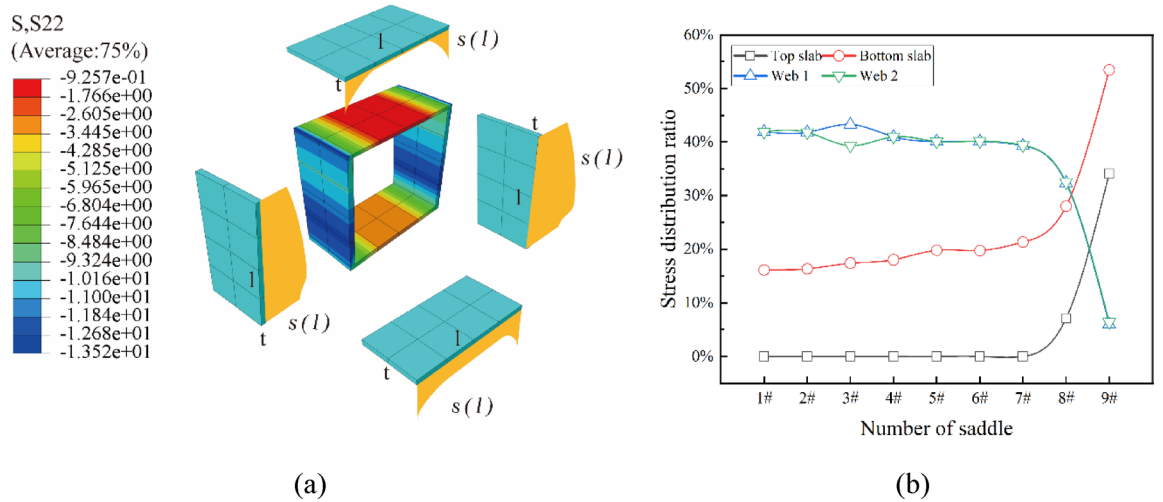


Fig. 13. Stress distribution ratio on the cable saddle surface. (a) Finite element schematic diagram (MPa), (b) Load distribution ratio.

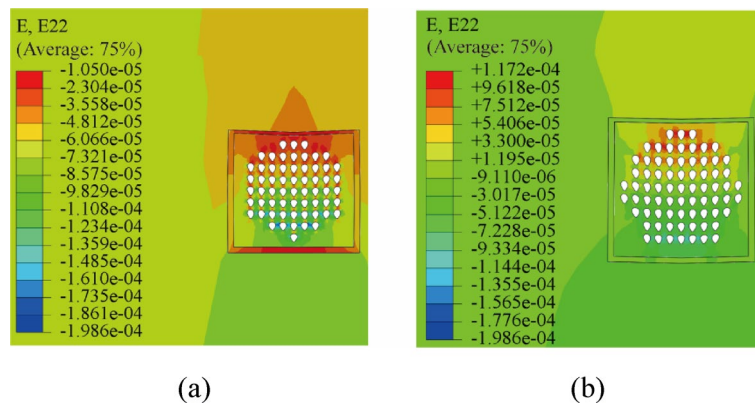


Fig. 14. Strain cloud diagram of filament hole. (a) 1# saddle, (b) 9# saddle.

For the 8# to 9# saddle seats, the load distribution ratio on the web plates decreases sharply, particularly in the 9# strand tube area, where the load distribution is only 6%. The load on the bottom plate increases to 53%. Due to the smaller distance from the tower top and the absence of external load effects above, the local deformation of the 9# saddle seat anchor zone is much greater than that of the concrete above the saddle, inducing vertical tensile stress in the concrete above the saddle. Consequently, the load carried by the top plate increases to 34%. When the tensile stress exceeds the bond strength between the top plate and the concrete, the steel plate at the top of the 9# strand tube saddle may detach from the concrete structure, which could affect the durability of the steel shell. This situation should be carefully considered in the design analysis.

Additionally, in the cross-section of the strand tube, due to the superposition effect of the cable forces, the compressive strain gradually increases. However, the relative deformation at the top is much greater than at the bottom. To ensure coordinated deformation between the grout and the steel shell, while the load is transmitted downward through the lower layers, it also acts on the web plates of the shell. Since the stiffness of the shell is significantly greater than that of the grout, based on the principle of stiffness distribution during load transfer, the web plates primarily bear the load, as shown in Fig. 14a. For the 8# to 9# strand tubes, the load is first distributed to the top plate to satisfy the coordinated deformation of the top of the saddle. Since the relative deformation on both sides is relatively small, the load distribution on the web plates significantly decreases, as shown in Fig. 14b.

Parameter sensitivity analysis

The reasonable selection of parameters plays a significant role in structural optimization design and improving engineering safety²¹. Previous studies have shown that the radius of the circular arc section has a significant impact on the stress distribution in the anchor zone. Furthermore, as demonstrated by the theoretical calculations in Sect. 2.2, the load distribution is related to both the cable force and the radius of the circular arc section. To investigate the effects of cable force and the radius of the cable saddle’s circular arc section on the stress in the

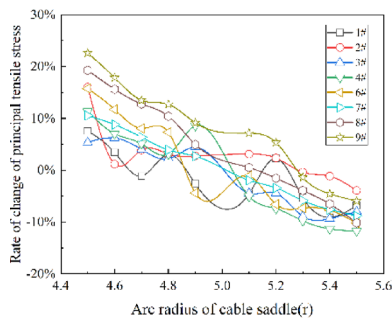
anchor zone, and to optimize the saddle design, a parameter analysis of the cable force and the radius of the circular arc section is conducted. This analysis provides a basis for on-site construction control.

To study the influence of the variation ratio of cable force λ (the ratio of the increase in cable force to the original cable force) and the curvature radius r of the cable saddle's circular arc segment on the spatial stress state in the bridge tower anchor zone, while keeping other parameters constant, λ is varied from 0 to 20% in 2% increments, and r is varied from 4.5 to 5.5 m in 0.1 m increments. The variation in the spatial stress in the key cross-sections of the concrete in the bridge tower anchor zone is examined. The results for the tensile stress in the high-strength grout, vertical stress in the concrete below the 1# strand saddle, and maximum principal tensile stress in the bridge tower are shown in Figs. 15, 16 and 17.

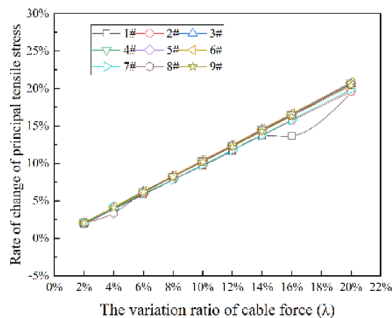
As shown in Fig. 15, the principal tensile stress in the high-strength grout for each strand tube varies similarly with the radius r of the cable saddle's circular arc segment. The tensile stress decreases gradually as the radius increases, and the absolute value of the stress increment is generally larger at $r=4.5$ m compared to $r=5.5$ m, where the rate of change slows down. Among these, the deviation in the rate of change for the 9# cable saddle is the most noticeable. At $r=4$ m, the rate of change is 22.6%, while at $r=5$ m, it is -6%. Since the load concentration q is linearly related to the cable force, the maximum principal stress in the high-strength grout of 1# saddle increases linearly with the increase in cable force increment ratio λ . This behavior can be explained by the fundamental mechanical relationship between the cable-grout interaction and structural design principles. The radial pressure transmitted from the stay cable to the grout is inversely proportional to the saddle arc radius r and directly proportional to the cable force parameter λ . In compliance with the Chinese railway design code, which mandates the use of the allowable stress method, the structure is required to behave linearly under all design load conditions. As a result, stress variations induced by load fluctuations can be accurately described using the principle of linear elasticity. It is this underlying mechanism that accounts for the characteristic decrease in principal tensile stress with increasing r and its linear increase with λ .

As seen in Fig. 16, the vertical stress in the concrete beneath the 1# saddle decreases with the increase in r under constant cable force, increasing r reduces the load concentration on the contact surface. At the same time, the length of the circular arc segment increases, and the vertical stress in the concrete beneath the saddle also decreases. The curves in the figure exhibit a relatively uniform layering distribution. In contrast, the vertical stress distribution in the linear section of the saddle is different. When $r \leq 5.1$ m, there is a noticeable stress concentration at the ends of the linear section, which significantly impacts local stress. As λ increases, the vertical stress beneath the 1# saddle shows a layered distribution with a clearly linear pattern.

As shown in Fig. 17, the principal tensile stress in the bridge tower is less affected by changes in the curvature of the cable saddle, but is more significantly influenced by changes in cable force. It generally varies linearly, with the maximum principal tensile stress located at the bifurcation point. According to linear calculations,

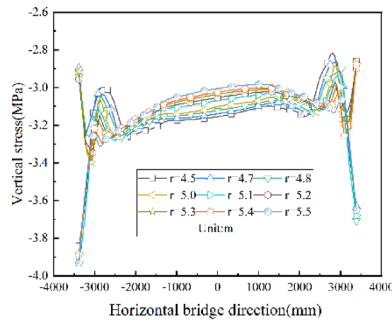


(a)

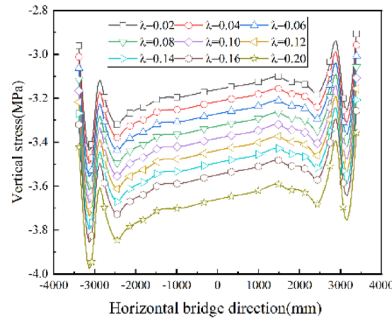


(b)

Fig. 15. Variation law of principal tensile stress in high-strength grout with respect to various parameters. (a) Curvature of the cable saddle arc segment, (b) The variation ratio of cable force.

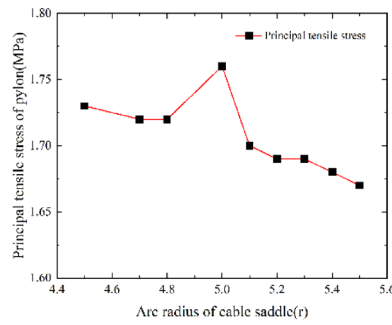


(a)

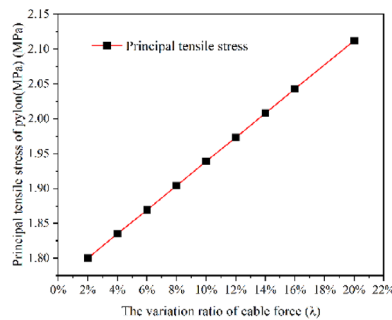


(b)

Fig. 16. Variation law of concrete vertical stress under saddle with respect to various parameters. (a) Curvature of the cable saddle arc segment, (b) the variation ratio of cable force.



(a)



(b)

Fig. 17. Variation law of maximum principal tensile stress of bridge tower with respect to various parameters. (a) Curvature of the cable saddle arc segment, (b) the variation ratio of cable force.



Fig. 18. The site construction of Changtu river bridge.

when $\lambda = 70\%$, the principal tensile stress at the bifurcation point reaches the allowable concrete stress value of 2.97 MPa, providing approximately 1.7 times the safety margin for the bridge tower structure.

The parameter analysis indicates that as the radius r of the arc segment decreases, the length of the curved section also reduces. According to the equivalent load calculation theory for the strand tube in Sect. 2.2, the load on the contact surface increases, which can lead to stress concentration, resulting in a significant rise in the principal tensile stress of the high-strength grout in the strand tube. At the same time, as the curved section shortens, stress diffusion is constrained, and the length of the linear section increases. Since the linear section does not directly bear the cable force, and the vertical distance between the saddles remains unchanged, this leads to an increased influence of the upper saddle on the stress in the lower saddle. Consequently, the vertical stress in the concrete beneath the saddle increases, exacerbating transverse cracking and raising the risk of concrete failure.

When the radius r of the arc segment falls within the 5–5.5 m range, the stress state of the saddle anchorage zone is more balanced. After considering the effects of the increased radius on the friction coefficient of the hole wall and the shortening of the linear section, it is recommended that the radius r of the saddle's arc segment be set within the 5–5.5 m range during the design phase. Additionally, both the principal tensile stress of the high-strength grout in the strand tube and the vertical stress in the concrete beneath the 1# saddle exhibit a linear increase as the cable force increment ratio λ rises. Within a 20% cable force increment range, the structure operates in an elastic state. Linear analysis further confirms that the bridge tower structure maintains a significant safety margin, offering valuable guidance for cable force control during construction.

Based on theoretical analysis and its implementation in engineering practice, the Changtu River Bridge has been successfully constructed. The Fig. 18 presents actual engineering photographs captured during the bridge erection process.

Conclusion

This study analyzes the spatial mechanical behavior of the anchorage zone in the Chongqing–Qianjiang high-speed railway Changtu River Bridge, a (132 + 132) m large-span curved T-shaped rigid-frame extradosed cable-stayed bridge. Using numerical simulations, the stress distribution and load transfer mechanisms were evaluated under operational conditions, focusing on the effects of cable force increment ratio λ and saddle arc curvature radius r . The key findings are as follows:

1. The maximum principal tensile and compressive stresses in the high-strength grout system are 5.01 MPa and -7.91 MPa, respectively, while the maximum Von Mises stress in the saddle steel shell reaches 16.27 MPa. In the bridge tower concrete, the maximum tensile and compressive stresses are 1.77 MPa and -5.085 MPa, respectively, all within the structural safety limits. However, a notable concentration of principal tensile stress occurs in the grout at the tower top, suggesting that material enhancement in this region may improve long-term performance. Additionally, the bifurcation point of the tower serves as a critical stress concentration zone, where additional reinforcement could be beneficial in mitigating potential cracking risks.
2. Longitudinally, the vertical stress in the saddle arc section remains uniform. Transversely, a layered diffusion effect is observed, with a localized transverse splitting stress of 0.11 MPa beneath the 1# saddle, which is well below the concrete's tensile design strength, indicating sufficient crack resistance. The transverse stress in the

concrete between saddles is influenced by the combined effect of both cable forces. In the 0.8–1.2 m range, the stress distribution follows an "M"-shaped pattern, while in the 0–0.8 m range, a "W"-shaped pattern emerges. This distribution highlights the complex interaction effects within the anchorage zone, emphasizing the need for careful stress management in structural design.

3. Cable forces are primarily transmitted through the web plates of the box-shaped steel shell to the bridge tower concrete. Each web plate carries approximately 40% of the total load, while the bottom plate supports around 20%. The top plate primarily experiences compressive stress from the upper concrete, with minimal direct contribution to cable force transfer. In the 9# saddle region, the web plate's load transfer ratio significantly decreases to 6%, while the bottom plate's share increases to 53%, and the top plate carries 34% of the load. In the absence of external loads above the saddle, local deformation in the anchorage area exceeds that of the upper concrete, inducing vertical tensile stress. This stress condition may lead to detachment between the saddle and tower concrete, potentially compromising the durability of the steel shell, requiring careful consideration in structural design.
4. The effects of key parameters, including the saddle arc radius r and cable force increment λ , reveal distinct trends in stress distribution. The principal tensile stress in the grout decreases as r increases, while it exhibits a linear increase with λ . The vertical stress in the concrete beneath the 1# saddle is inversely proportional to r and directly proportional to λ . The highest lateral splitting stress occurs at the bifurcation point, which remains independent of r but positively correlated with λ . A more favorable stress distribution is observed when r falls within the range of 5–5.5 m. When λ reaches 70%, the principal tensile stress approaches its allowable limit, ensuring a safety margin of 1.7 times, thus confirming the structural adequacy for operational conditions.

Future research could focus on experimental validation through scaled model tests to verify numerical findings under realistic loading conditions. Additionally, long-term performance evaluation is essential to assess the fatigue behavior and durability of high-strength grout and the saddle's steel shell under sustained loads. Further optimization of saddle design could refine structural parameters to improve load transfer efficiency and mitigate stress concentrations. This study provides a comprehensive assessment of the anchorage zone mechanics in extradosed cable-stayed bridges, offering practical guidance for the design and construction of similar structures.

Data availability

Correspondence and requests for materials should be addressed to Mingzhi XIE.

Received: 11 May 2025; Accepted: 19 September 2025

Published online: 27 October 2025

References

1. Gao, Z. Zhengzhou Yellow River road-cum-railway bridge, China. *Stahlbau* **81**, 151–155 (2012).
2. Li, H. et al. Numerical and experimental investigation of an extradosed cable-stayed bridge in urban rail transit under dynamic train load. *Int. J. Struct. Stab. Dyn.* **24**, 2541014 (2024).
3. Zhihua, X. et al. Structural performance and cost analysis of multi-span extradosed cable-stayed bridge. *Int. Assoc. Bridge Struct. Eng.* <https://doi.org/10.2749/nanjing.2022.0387> (2022).
4. Collings, D. & Gonzalez, A. S. Extradosed and cable-stayed bridges, exploring the boundaries. *Proc. Inst. Civ. Eng. Bridge Eng.* **166**, 231–239 (2013).
5. Niu, Y. et al. Experimental study of the anti-slip capacity of saddle-type pylon anchorage for extradosed bridges. *J. Comput. Theor. Nanosci.* **13**, 1486–1493 (2016).
6. Song, T. et al. Predicting the ultimate load capacity of extradosed cable-stayed bridges: A novel method. *KSCE J. Civ. Eng.* **28**, 2863–2871 (2024).
7. Chen, X., Liu, Z., & Wang, C. Nonlinear stress analysis of cable-pylon anchorage zones RC of extra-dosed cable-stayed bridge in railway. In: *Proceeding of 6th International Conference on Measuring Technology Mechatronics Automation. IEEE*, pp. 430–434 (2014).
8. Du, Z. et al. Strong-weak zone model and test of sleeves in anchorage component of extradosed cable-stayed bridge. *Sci. Technol. Eng.* **23**, 12679–12686 (2023).
9. Xu, Q. et al. Experimental study on saddle with diamond-shaped single-wire pipes for steel strand cables of low-pylon cable-stayed bridge. *Highway* **64**, 160–163 (2019).
10. Ni, S. Study on the anchorage zone structure of pylons in low-pylon cable-stayed bridges. Master's thesis, *Huazhong Univ. Sci. Technol.* (2022).
11. Shan, J. et al. Development and application of saddle for steel strand cables of low-pylon cable-stayed bridge. *Highway* **62**, 132–135 (2017).
12. Li, J. et al. Full-scale model experimental study of the HDPE multitube saddle of an extradosed bridge. *Struct. Eng. Int.* **32**, 527–537 (2022).
13. Wang, L. et al. Behavior of multispan extradosed bridge subjected to variation of cable-free segment length. *J. Eng.* **2022**, 7555127 (2022).
14. Chehrizi, A. et al. Probabilistic fretting fatigue analysis of bridge stay cables at saddle supports. *Struct. Eng. Int.* **30**, 571–579 (2020).
15. Tang, Y., Li, Y., Niu, Y., et al. Finite difference method in stress analysis of anchorage zone of highway extradosed cable-stayed bridge. In: *MATEC Web Conference : International Conference on Civil Engineering and Material Science. (ICCEMS)* **206**, 01007 (2018).
16. Niu, Y. et al. The research of space temperature distribution in solid tower of extradosed cable-stayed bridge. *J. Civ. Eng. Sci. Technol.* <https://doi.org/10.2174/1874836801408010488> (2014).
17. Lou, D. et al. Analytical determination of static deflection shape of an asymmetric extradosed cable-stayed bridge using Ritz method. *Materials* **15**, 4255 (2022).
18. Liu, Z. et al. Study of mechanical characteristics for strand deviating saddle zone of extradosed cable-stayed bridge. *Bridge Constr.* **48**, 69–74 (2018).
19. Tang, Y. et al. Splitting limit behavior analysis and model test of sub-tube cable-to-pylon anchorage zone. *J. Chang'an Univ. (Nat. Sci. Ed.)* **38**, 127–134 (2018).

20. Lin, S. et al. Analysis of crack resistance of saddle for extradosed bridge based on extended finite element method. *Bridge Constr.* **45**, 68–73 (2015).
21. Xie, M. et al. Probabilistic seismic sensitivity analyses of high-speed railway extradosed cable-stayed bridges. *Appl. Sci.* **13**, 7036. <https://doi.org/10.3390/app13127036> (2023).

Acknowledgements

This research was supported by the Sichuan Science and Technology Program (2020YJ0081), the National Natural Science Foundation of China (52322811) and the National Science Foundation of China (No.52178169)

Author contributions

M.X. and K.W. wrote the main manuscript text. S.G. and X.L. did research on the literature. Z.Y. and W.B. prepared figures. All authors reviewed the manuscript.

Declarations

Competing interests

The authors declare no competing interests.

Additional information

Correspondence and requests for materials should be addressed to M.X.

Reprints and permissions information is available at www.nature.com/reprints.

Publisher's note Springer Nature remains neutral with regard to jurisdictional claims in published maps and institutional affiliations.

Open Access This article is licensed under a Creative Commons Attribution-NonCommercial-NoDerivatives 4.0 International License, which permits any non-commercial use, sharing, distribution and reproduction in any medium or format, as long as you give appropriate credit to the original author(s) and the source, provide a link to the Creative Commons licence, and indicate if you modified the licensed material. You do not have permission under this licence to share adapted material derived from this article or parts of it. The images or other third party material in this article are included in the article's Creative Commons licence, unless indicated otherwise in a credit line to the material. If material is not included in the article's Creative Commons licence and your intended use is not permitted by statutory regulation or exceeds the permitted use, you will need to obtain permission directly from the copyright holder. To view a copy of this licence, visit <http://creativecommons.org/licenses/by-nc-nd/4.0/>.

© The Author(s) 2025